

# A SBFEM formula for the mixed-order hexahedron interpolation based on serendipity elements

Xiupeng Nie<sup>a,b</sup>, Degao Zou<sup>a,b</sup>, Kai Chen<sup>a,b,\*</sup>, Xianjing Kong<sup>a,b</sup>, Guoyang Yi<sup>a,b</sup>

<sup>a</sup> The State Key Laboratory of Coastal and Offshore Engineering, Dalian University of Technology, Dalian, Liaoning 116024, China

<sup>b</sup> School of Hydraulic Engineering, Dalian University of Technology, Dalian, Liaoning 116024, China

## ARTICLE INFO

### Keywords:

Scaled boundary element method  
Mixed-order interpolation  
Hexahedron elements  
Order conversion

## ABSTRACT

The hexahedron elements have been widely used in theoretical research and engineering applications because of their simple formulation and fine analytical performance. In this paper, a flexible mixed-order hexahedron interpolation is proposed based on the SBFEM theory, which is summarized as follows: (1) The interpolation functions are constructed for boundary surfaces by introducing the “Serendipity element”, which allows for a combination of linear and quadratic interpolation; (2) Two approaches for order conversion in hexahedron elements have been applied and investigated; (3) The accuracy and applicability of the proposed method are verified using several classical examples and engineering practice. In this way, the proposed method is capable of handling abundant patterns of different order combinations, thus the analysis performance of hexahedron elements has been improved. The precision of the proposed method is demonstrated by comparing it with the theoretical solution and the classical isoparametric FEM. By comparison, the computational efficiency can be improved by approximately 40–55 % with satisfactory accuracy. In general, the proposed method offers a new alternative channel for simulating particular problems, such as bending and stress concentration.

## 1. Introduction

The finite element method (FEM) is a prominent numerical analysis technique widely used in modern engineering practice. This numerical technique introduces the concept of discretization to partition complex geometric domains into a finite number of simplex subdomains, its simulation process is practical and easy to implement, which has attracted a great deal of attention from researchers in recent years. However, the accuracy of FEM analysis is greatly influenced by the quality and shape of the discretized mesh. Therefore, the selection of suitable element types and mesh discretization schemes is essential to ensure the accuracy of FEM analysis.

The conventional element types in 3D finite element analysis are generally limited to tetrahedron or hexahedron elements. Other types of elements, such as pentahedron elements, can also be generated by degenerating hexahedron elements [1]. Tetrahedron meshes are easier to discretize than hexahedron meshes, however, it is known that the tetrahedron element lacks capability in stress analysis [2,3]. In contrast to the tetrahedron element, the well-established hexahedron element is preferred by researchers for its solution accuracy [4,5] and computational stability. Besides, it also possesses the characteristic of being easy

to formulate [6]. Benefiting from these advantages, hexahedron elements have gained increasingly wide utilization in various fields of FEM analysis, such as crack propagation [7,8], discontinuous deformation analysis [6,9], adaptive mesh refinement analysis [10], diffusion and transient reaction-diffusion [11].

To accurately capture the mechanical behavior of the structure, a class of numerical simulations represented by the fined analysis has been carried out successively, which undoubtedly imposes more stringent demands on the high quality and universality of the mesh discretization. Due to their computational stability and simplicity, linear hexahedron elements are commonly applied in fined theoretical and engineering research and have yielded satisfactory simulation results [12–14]. However, in specific research scenarios, such as bending problems or localized stress concentration problems, the linear form of elements may lead to simulation distortion because the calculated bending stiffness is too rigid [15]. Additionally, it cannot accurately describe rapidly changing stress gradients [16], making it challenging to perform well in FEM analysis of the aforementioned issues. On the contrary, the quadratic hexahedron elements are better equipped to handle the above problems [17]. However, the number of degrees of freedom (Dofs) in a quadratic element will be doubled, leading to a significant increase in

\* Corresponding author.

E-mail address: [chenkai@dlut.edu.cn](mailto:chenkai@dlut.edu.cn) (K. Chen).

<https://doi.org/10.1016/j.enganabound.2024.105760>

Received 8 January 2024; Received in revised form 24 April 2024; Accepted 25 April 2024

Available online 2 May 2024

0955-7997/© 2024 Elsevier Ltd. All rights reserved.

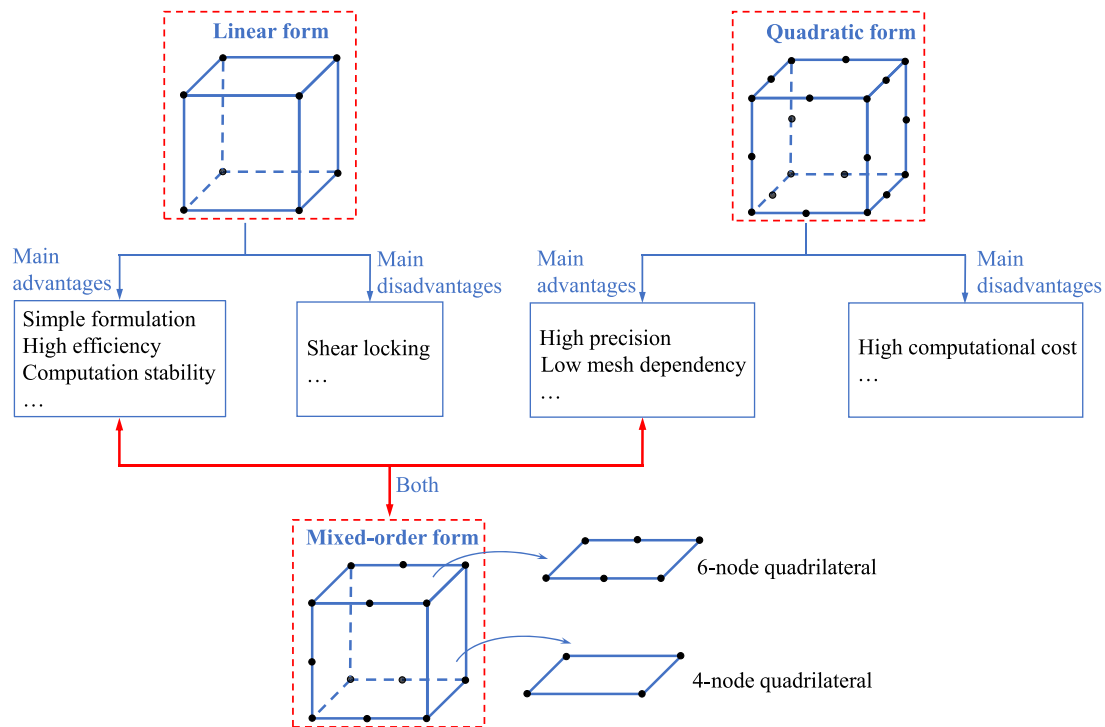


Fig. 1. Schematic diagram of the mixed-order hexahedron element.

the computational effort for the entire problem domain.

To achieve a fine balance between computational accuracy and efficiency of the element, researchers have explored several approaches, including the non-conforming element [18], the reduced integration scheme [19], and the serendipity element [20]. The non-conforming element provides accurate displacement and stress results by adding incompatible quadratic displacement terms to linear compatible terms [21]. However, its analytical accuracy may be compromised if the elements in the interest region are severely distorted [22]. Reduced integration improves computational efficiency by using fewer integration points in the quadratic element, yet this approach tends to result in stress solutions with relatively low accuracy [23]. The serendipity element allows 2D quadrilateral elements to be equipped with linear or quadratic orders on each edge, thereby achieving compatibility of mixed orders in a single element [24,25]. However, its implementation process and potential computational benefits in FEM have proven to be a major challenge [26].

In addition to the above methods, a new semi-analytical analysis method called the scaled boundary finite element method (SBFEM) has been proposed by Wolf and Song [27] in recent years. The solutions of SBFEM are numerical in the circumferential direction and analytical in the radial direction, making it easy to construct polygon elements with high accuracy. After recent developments, the SBFEM theory has been systematically established as a mature numerical analysis method by Song [28–30], and abundant research works have also been conducted by researchers. This paper briefly lists some representative research studies. For example, Zhang et al. [31–33] proposed a structural dynamic analysis method based on SBFEM, which has been demonstrated to have high performance for engineering applications. Du et al. [34–36] utilized SBFEM to address the challenges of static and dynamic crack initiation and propagation, providing a more realistic description of the local crack damage zone. Zhao et al. [37–40] proposed a novel time-domain numerical method for SBFEM to analyze wave propagation problems, and efficient and practical solutions with great application potential for analyzing interactions between engineering structures have been obtained. Guo et al. [41,42] conducted topology optimization analysis using SBFEM, and the results showed good improvements in

computational efficiency and process simplification. Liu et al. [43,44] developed a new isogeometric SBFEM for piezoelectric laminates and cylindrical shells. Researchers have also conducted research on SBFEM in various fields, such as 2D Cosserat continuum analysis [45], nonlinear analysis in complex geotechnical engineering [46,47], transient analysis of elastic wave propagation [48], direct numerical analysis of point-cloud models [49], and adaptive mesh refinement analysis [50, 51]. A newly developed 2D “mixed-order” polygon element, which has been preliminarily proposed by Chen et al. [52] by means of SBFEM, enables the flexible combination of linear and quadratic forms of edges within a polygon element. In this way, the high accuracy and efficiency of elements in the calculation can be effectively ensured.

To achieve compatibility of high-precision and efficient analysis in hexahedron elements, this paper proposes a flexible mixed-order hexahedron element within the framework of SBFEM, which allows for the free combination of linear and quadratic forms of the element’s edges. Combined with serendipity element interpolation functions, each surface of the hexahedron element is interpolated in the manner of FEM. Besides, two order conversion approaches are applied based on the critical regions and flexural angle of each edge in elements. Finally, the accuracy and effectiveness of the proposed method are demonstrated through several examples for different problems.

This paper is organized as follows. In Section 2, the mixed-order hexahedron element based on serendipity elements is introduced. Section 3 briefly the SBFEM formulation for the mixed-order hexahedron element. A classic numerical example is presented in Section 4 to verify the accuracy and effectiveness of the proposed method, meanwhile, the remaining two examples are applied to demonstrate the proposed two order conversion approaches. In Section 5, the applicability of the proposed method is illustrated through an engineering practice. Finally, conclusions are stated in Section 6.

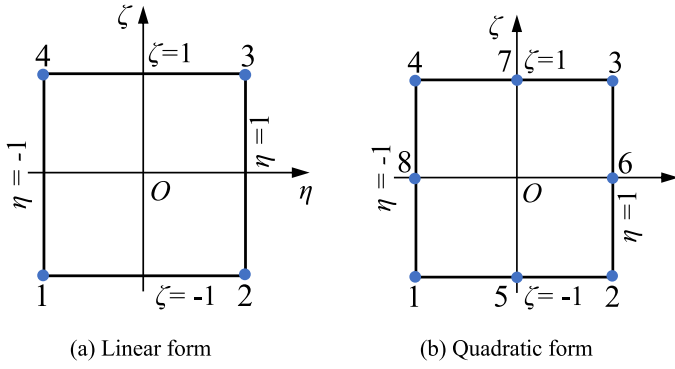


Fig. 2. Quadrilateral iso-parametric element.

## 2. The mixed-order hexahedron element based on serendipity elements

### 2.1. Introduction of the mixed-order hexahedron element

Since the linear and quadratic forms of hexahedron elements have their advantages and disadvantages, a new form of the hexahedron element with both advantages can be constructed, and its schematic diagram is depicted in Fig. 1. As can be seen, the linear and quadratic form of edges in the hexahedron element is selectively assigned, hence it is called “mixed-order” element. The specific order allocation principles for each edge will be explored in the following content. Each surface conforms to quadrilateral elements with 4–8 nodes, which can be interpolated through serendipity elements, and its relevant details are given below.

### 2.2. Summary of the serendipity elements

#### 2.2.1. The serendipity elements and standardization

In planar problems, 4-node and 8-node quadrilateral elements are commonly more favored, whose iso-parametric forms are shown in Fig. 2. However, other variable node element types, i.e., 5–7 node elements, will occur in the mixed-order elements shown in Fig. 1. Based on 2D quadrilateral iso-parametric element, 16 types of quadrilateral serendipity elements with different numbers of nodes can be included, as shown in Fig. 3.

For elements with 5–7 nodes, there are multiple types of corresponding interpolation functions due to the varying distribution locations of nodes. For these types of elements, a standardization process has been performed, as shown in Fig. 3. The serendipity elements with 5–7 nodes can be normalized to a standardized element by altering the arrangement order of the first node, provided that such elements have the same number of nodes. Through this process, the types of serendipity elements can be reduced to 6. By this means, the efficiency of the computational process can be significantly improved.

#### 2.2.2. Interpolation function

The interpolation function of linear and quadratic quadrilateral iso-parametric elements, as shown in Fig. 1, can be referred to [18,53]. Based on the interpolation functions of these two iso-parametric element types, the interpolation functions of serendipity elements with different nodes can be derived, as listed in Table 1.

In Table 1, the interpolation functions  $N_1$ – $N_4$  in column 2 are shape functions at corner nodes of the linear quadrilateral element, and  $N_5$ – $N_8$  represents the edge midpoint shape functions of the quadratic quadrilateral element. It is proved that all the above-formed interpolation functions of serendipity elements with 4–8 nodes satisfy Lagrange

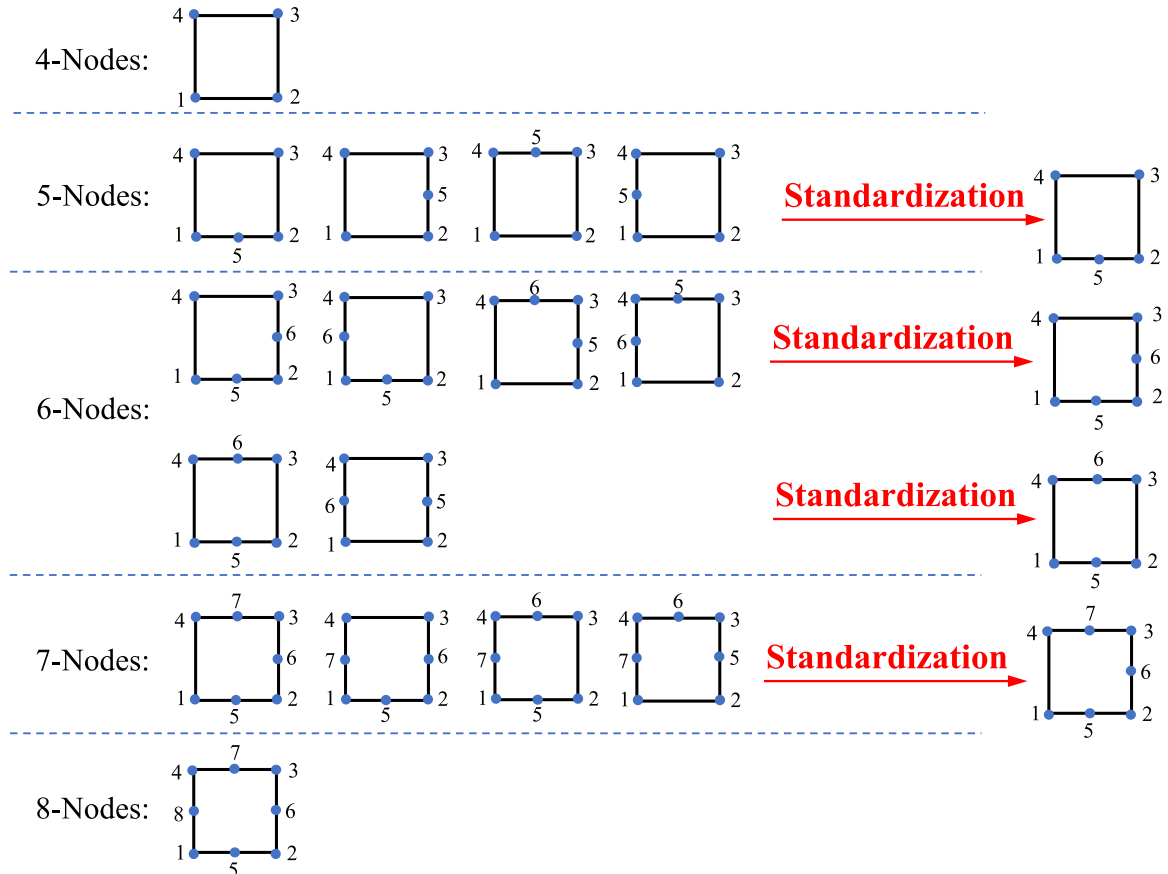


Fig. 3. Different types of the serendipity elements and standardization process.

**Table 1**

Uniform interpolation function for serendipity elements with 4 - 8 nodes.

$N_i$	Interpolation function	The following items will only be included when the node $i$ exists			
		$i = 5$	$i = 6$	$i = 7$	$i = 8$
$N_1 =$	$\frac{1}{4}(1 - \eta)(1 - \zeta)$	$-\frac{1}{2}N_5$			$-\frac{1}{2}N_8$
$N_2 =$	$\frac{1}{4}(1 + \eta)(1 - \zeta)$	$-\frac{1}{2}N_5$	$-\frac{1}{2}N_6$		
$N_3 =$	$\frac{1}{4}(1 + \eta)(1 + \zeta)$		$-\frac{1}{2}N_6$	$-\frac{1}{2}N_7$	
$N_4 =$	$\frac{1}{4}(1 - \eta)(1 + \zeta)$			$-\frac{1}{2}N_7$	$-\frac{1}{2}N_8$
$N_5 =$	$\frac{1}{2}(1 - \eta^2)(1 + \zeta)$				
$N_6 =$	$\frac{1}{2}(1 - \eta)(1 - \zeta^2)$				
$N_7 =$	$\frac{1}{2}(1 - \eta^2)(1 - \zeta)$				
$N_8 =$	$\frac{1}{2}(1 + \eta)(1 - \zeta^2)$				

properties, i.e., non-negative functions, the partition of unity, and Kronecker-delta.

### 3. SBFEM formula for mixed-order hexahedron element

#### 3.1. 3D scaled boundary coordinate

In the context of SBFEM, a 3D mixed-order hexahedron domain and its boundaries can be discretized into any  $n$ -node hexahedron, as shown in Fig. 4. A scale center, represented as  $O$  with coordinates  $(x_0, y_0, z_0)$ , is introduced inside the domain, ensuring that any point on the hexahedron boundary is directly visible from the point  $O$ . For this 3D domain, the boundary  $S$  of domain  $V$  is discretized with quadrilateral surface elements. Fig. 4(a) shows a typical serendipity surface element with 6 nodes on the upper boundary  $S_{top}$ , and the corresponding parent element is displayed in Fig. 4(b).

In the scaled boundary coordinate, a coordinate system similar to FEM  $(\xi, \eta, \zeta)$  is introduced, among which  $\xi$  represents the radial coordinate,  $\eta$  and  $\zeta$  are the circumferential coordinates. The boundary is then scaled by the normalized radial coordinate  $\xi$ , which has a zero value at the center of the scale and a unity value on the boundary. The boundaries of the domain are discretized using a simple 2D FEM by the formalized interpolation function  $N(\eta, \zeta)$  of serendipity elements in the local coordinates  $\eta$  and  $\zeta$ . The point in the Cartesian coordinate system  $\{x, y, z\}$  can be represented by the scaled boundary coordinates  $(\xi, \eta, \zeta)$  as:

$$\begin{aligned} x(\xi, \eta, \zeta) &= x_0 + \xi N(\eta, \zeta) \\ y(\xi, \eta, \zeta) &= y_0 + \xi N(\eta, \zeta) \\ z(\xi, \eta, \zeta) &= z_0 + \xi N(\eta, \zeta) \end{aligned} \quad (3.1)$$

In the conversion process of scaled boundary coordinates, a standard procedure similar to FEM is used to achieve the conversion. The

Jacobian matrix and determinant on the boundary are shown in Eq. (3.2).

$$J(\eta, \zeta) = \begin{bmatrix} x(\eta, \zeta) & y(\eta, \zeta) & z(\eta, \zeta) \\ x(\eta, \zeta)_{,\eta} & y(\eta, \zeta)_{,\eta} & z(\eta, \zeta)_{,\eta} \\ x(\eta, \zeta)_{,\zeta} & y(\eta, \zeta)_{,\zeta} & z(\eta, \zeta)_{,\zeta} \end{bmatrix} \quad (3.2)$$

$$|J(\eta, \zeta)| = x(y_{,\eta}z_{,\zeta} - z_{,\eta}y_{,\zeta}) + y(z_{,\eta}x_{,\zeta} - x_{,\eta}z_{,\zeta}) + z(x_{,\eta}y_{,\zeta} - y_{,\eta}x_{,\zeta}) \quad (3.3)$$

where the derivatives are expressed as:

$$\begin{aligned} x(\eta, \zeta)_{,\eta} &= N(\eta, \zeta)_{,\eta} \cdot x, & x(\eta, \zeta)_{,\zeta} &= N(\eta, \zeta)_{,\zeta} \cdot x \\ y(\eta, \zeta)_{,\eta} &= N(\eta, \zeta)_{,\eta} \cdot y, & y(\eta, \zeta)_{,\zeta} &= N(\eta, \zeta)_{,\zeta} \cdot y \\ z(\eta, \zeta)_{,\eta} &= N(\eta, \zeta)_{,\eta} \cdot z, & z(\eta, \zeta)_{,\zeta} &= N(\eta, \zeta)_{,\zeta} \cdot z \end{aligned} \quad (3.4)$$

#### 3.2. SBFEM theory formulation

The relationship between the displacements and strains in elastic theory is written as

$$\varepsilon = Lu \quad (3.5)$$

The displacement field in the SBFEM can be approximated as

$$u(\xi, \eta, \zeta) = N_u(\eta, \zeta)u(\xi) \quad (3.6)$$

where  $u(\xi)$  is the displacement along the radial direction  $\xi$ , the shape functions  $N_u(\eta, \zeta)$  is expressed as  $[N_1(\eta, \zeta)I, N_2(\eta, \zeta)I, \dots]$ ,  $I$  is a  $3 \times 3$  identity matrix. The linear differential operator in 3D is written in the  $(\xi, \eta, \zeta)$  coordinates as:

$$L = b_1 \frac{\partial}{\partial \xi} + \frac{1}{\xi} \left( b_2 \frac{\partial}{\partial \eta} + b_3 \frac{\partial}{\partial \zeta} \right) \quad (3.7)$$

where  $b_1(\eta, \zeta)$ ,  $b_2(\eta, \zeta)$  and  $b_3(\eta, \zeta)$  are defined as:

$$b_1(\eta, \zeta) = \frac{1}{|J|} \begin{bmatrix} y_{,\eta}z_{,\zeta} - z_{,\eta}y_{,\zeta} & 0 & 0 \\ 0 & z_{,\eta}x_{,\zeta} - x_{,\eta}z_{,\zeta} & 0 \\ 0 & 0 & x_{,\eta}y_{,\zeta} - y_{,\eta}x_{,\zeta} \\ 0 & x_{,\eta}y_{,\zeta} - y_{,\eta}x_{,\zeta} & z_{,\eta}x_{,\zeta} - x_{,\eta}z_{,\zeta} \\ x_{,\eta}y_{,\zeta} - y_{,\eta}x_{,\zeta} & 0 & y_{,\eta}z_{,\zeta} - z_{,\eta}y_{,\zeta} \\ z_{,\eta}x_{,\zeta} - x_{,\eta}z_{,\zeta} & y_{,\eta}z_{,\zeta} - z_{,\eta}y_{,\zeta} & 0 \end{bmatrix} \quad (3.8)$$

$$b_2(\eta, \zeta) = \frac{1}{|J|} \begin{bmatrix} zy_{,\zeta} - yz_{,\zeta} & 0 & 0 \\ 0 & xz_{,\zeta} - zx_{,\zeta} & 0 \\ 0 & 0 & yx_{,\zeta} - xy_{,\zeta} \\ 0 & yx_{,\zeta} - xy_{,\zeta} & xz_{,\zeta} - zx_{,\zeta} \\ yx_{,\zeta} - xy_{,\zeta} & 0 & zy_{,\zeta} - yz_{,\zeta} \\ xz_{,\zeta} - zx_{,\zeta} & zy_{,\zeta} - yz_{,\zeta} & 0 \end{bmatrix} \quad (3.9)$$

$$b_3(\eta, \zeta) = \frac{1}{|J|} \begin{bmatrix} yz_{,\eta} - zy_{,\eta} & 0 & 0 \\ 0 & zx_{,\eta} - xz_{,\eta} & 0 \\ 0 & 0 & xy_{,\eta} - yx_{,\eta} \\ 0 & xy_{,\eta} - yx_{,\eta} & zx_{,\eta} - xz_{,\eta} \\ xy_{,\eta} - yx_{,\eta} & 0 & yz_{,\eta} - zy_{,\eta} \\ zx_{,\eta} - xz_{,\eta} & yz_{,\eta} - zy_{,\eta} & 0 \end{bmatrix} \quad (3.10)$$

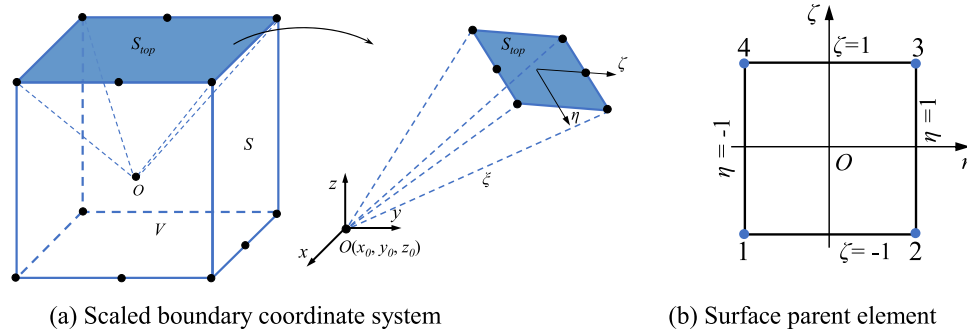


Fig. 4. 3D scaled boundary coordinates in a mixed-order hexahedron element.

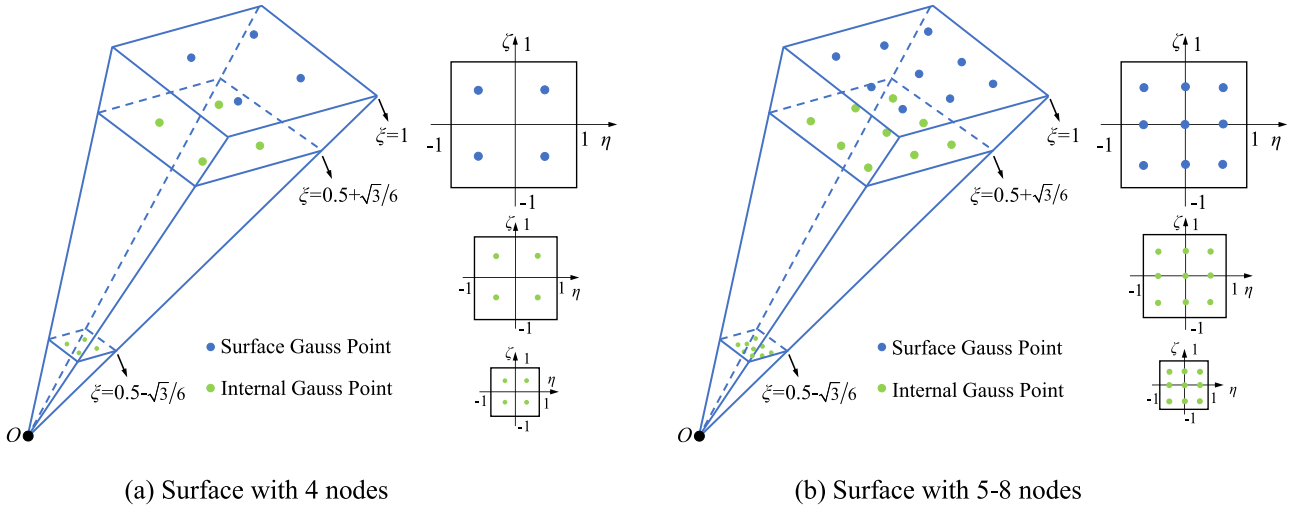


Fig. 5. Distribution of internal Gauss integral points for different surfaces.

The strain field in the scaled boundary coordinates can be obtained by combined Eqs. (3.5) - (3.7), and it is expressed as

$$\varepsilon = B_1 u(\xi)_{,\xi} + \frac{1}{\xi} B_2 u(\xi) \quad (3.11)$$

The stress field in the scaled boundary coordinates is further obtained as

$$\sigma = D \left( B_1 u(\xi)_{,\xi} + \frac{1}{\xi} B_2 u(\xi) \right) \quad (3.12)$$

where  $D$  is the elastic matrix.  $B_1$  and  $B_2$  are the standard scaled boundary finite element strain-displacement matrices, which are written as

$$\begin{aligned} B_1 &= b_1 N_u(\eta, \zeta) \\ B_2 &= b_2 N_u(\eta, \zeta)_{,\eta} + b_3 N(\eta, \zeta)_{,\zeta} \end{aligned} \quad (3.13)$$

Based on the virtual work principle [54], the governing equation in terms of displacement without external load for 3D SBFEM can be expressed as

$$E_0 \xi^2 u(\xi)_{,\xi\xi} + (2E_0 + E_1^T - E_1) \xi u(\xi)_{,\xi} + (E_1^T - E_2) u(\xi) = 0 \quad (3.14)$$

$E_0$ ,  $E_1$ , and  $E_2$  are the coefficient matrices in the scaled boundary coordinates that depend on the geometry and the material properties of the subdomain, which are defined as follows:

$$\begin{aligned} E_0 &= \int_{-1}^1 \int_{-1}^1 B_1^T D B_1 |J| d\eta d\zeta \\ E_1 &= \int_{-1}^1 \int_{-1}^1 B_2^T D B_1 |J| d\eta d\zeta \\ E_2 &= \int_{-1}^1 \int_{-1}^1 B_2^T D B_2 |J| d\eta d\zeta \end{aligned} \quad (3.15)$$

By introducing a variable  $X(\xi)$ , whose formulation is given in Eq. (3.16), Eq. (3.14) can be converted to a first-order homogeneous differential equation, just as shown in Eq. (3.17).

$$X(\xi) = \begin{bmatrix} \xi^{0.5} u(\xi) \\ \xi^{-0.5} q(\xi) \end{bmatrix} \quad (3.16)$$

$$\xi X(\xi)_{,\xi} = -Z X(\xi) \quad (3.17)$$

where  $q(\xi)$  is the internal nodal force vector, the Hamilton matrix  $Z$  is expressed as

$$Z = \begin{bmatrix} E_0^{-1} E_1^T - 0.5I & -E_0^{-1} \\ -E_2 + E_1 E_0^{-1} E_1^T & -(E_1 E_0^{-1} - 0.5I) \end{bmatrix} \quad (3.18)$$

Eigenvalue decomposition is performed on the Hamiltonian matrix  $Z$ , and the Eq. (3.19) at the element level is derived.

$$Z \begin{bmatrix} \psi_u \\ \psi_q \end{bmatrix} = \begin{bmatrix} \psi_u \\ \psi_q \end{bmatrix} S_n \quad (3.19)$$

where  $S_n$  is a diagonal matrix composed of the real parts of the eigenvalues generated from the decomposition of the  $Z$  matrix.  $\psi_u$  and  $\psi_q$  are the modal displacements and forces, respectively. Therefore, the general solutions for the displacements  $u(\xi)$  and internal nodal forces  $q(\xi)$  of Eq. (3.14) for the hexahedron element are

$$\begin{aligned} u(\xi) &= \psi_u \xi^{-(S_n+0.5I)c} \\ q(\xi) &= \psi_q \xi^{-(S_n-0.5I)c} \end{aligned} \quad (3.20)$$

where  $I$  is the identity matrix, and  $c$  is an integral constant matrix, which can be obtained from the node displacement  $u_b$  on the subdomain boundary:

$$c = \psi_u^{-1} u_b \quad (3.21)$$

Then, the displacement field  $u(\xi, \eta, \zeta)$  inside the hexahedron element is obtained by substituting Eq. (3.20) into Eq. (3.6):

$$u(\xi, \eta, \zeta) = N_u(\eta, \zeta) \psi_u \xi^{-(S_n+0.5I)c} \psi_u^{-1} u_b \quad (3.22)$$

Therefore, in the form of FEM, the element shape functions  $\Phi(\xi, \eta, \zeta)$  is extracted as:

$$\Phi(\xi, \eta, \zeta) = N_u(\eta, \zeta) \psi_u \xi^{-(S_n+0.5I)c} \psi_u^{-1} \quad (3.23)$$

The strain field of a hexahedron element can be derived by substituting Eqs. (3.7) and (3.22) into Eq. (3.5):

$$\varepsilon(\xi, \eta, \zeta) = [B_1 \psi_u (-S_n - 0.5) + B_2 \psi_u] \xi^{-(S_n+1.5I)c} \psi_u^{-1} u_b \quad (3.24)$$

$$B_u = [B_1 \psi_u (-S_n - 0.5) + B_2 \psi_u] \xi^{-(S_n+1.5I)c} \psi_u^{-1} \quad (3.25)$$

### 3.3. Gauss integral point scheme

Since SBFEM is only discrete on the boundary, the Gauss integral point is also limited to the boundary surface. However, these Gauss points cannot accurately describe the nonlinear properties within the element, which greatly restricts the application of SBFEM in the field of nonlinear analysis. To enhance the nonlinear capability of SBFEM and make it applicable to engineering practice, a mixed internal Gauss integral point scheme is adopted in the mixed-order hexahedron element.

In this scheme, the Gauss integration rule is used to determine the

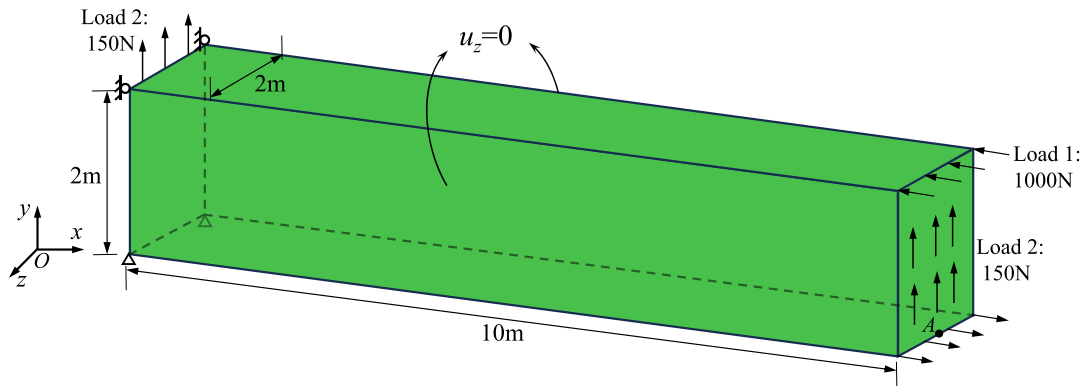


Fig. 6. Classical cantilever beam model.

position of integral points in the hexahedron element domain. By connecting the scaled center  $O$  and the nodes in the circumferential boundary, the hexahedron can be divided into six pyramidal subdomains. A representative pyramid is shown in Fig. 5. For 4-node surface elements,  $2 \times 2$  Gauss points on the interface are selected according to the Gauss integration rule. By scaling the Gauss points on the interface, the distribution of internal Gauss points is shown in Fig. 5, which is located on the planes with radial directions  $0.5 \pm \sqrt{3}/6$ . Through this manner, a total of 8 internal Gauss points is determined. Similarly, for surface elements with 5–8 nodes,  $3 \times 3$  interface Gauss points are determined, followed by 18 internal Gauss points, thus the mixed integral scheme is constructed.

#### 4. Numerical example

##### 4.1. Verification of the effectiveness and accuracy

###### 4.1.1. The cantilever beam example

For effectiveness and accuracy verification, a classical cantilever beam subjected to bending, which has been analyzed in [18], is considered in this section. The detailed dimensions and properties are described in Fig. 6. The material properties are Young's modulus  $E = 1500$  Pa, and Poisson's ratio  $\nu = 0.25$ . Two different loadings are applied, as shown in Fig. 6, whereby the bending behavior will be generated through the loadings.

The model is first discretized by the quadratic hexahedron element, and a total of 250 elements and 1416 nodes are yielded. The 3D mesh is shown in Fig. 7(a). In addition, a mesh with mixed-order elements is constructed, in which the lines in red represent the quadratic line elements and blues are linear forms, just as shown in Fig. 7(b). When the free end of this cantilever beam is subjected to the above loadings, the horizontal edges of the element will undergo obvious bending deformation, so these edges are adopted as high-precision quadratic forms. Conversely, the vertical edges of the beam are slightly bending, thus all vertical edges are considered as linear forms. In addition, for comparison, a mesh with linear edges is adopted, as shown in Fig. 7(c).

###### 4.1.2. Results comparison

Numerical simulation calculations for different element types are performed, the detailed information can be found in Table 2. Noteworthy, Hex8 corresponds to the linear mesh in Fig. 7(c), Hex20 represents the quadratic mesh in Fig. 7(a), and SBFEM-M is the mixed-order mesh in Fig. 7(b). The computer software GEODYNA 8.0 [55], which integrates various numerical analysis methods such as SBFEM and FEM, is used to perform the calculations provided in Table 2.

The displacement component- $y$  of point A is observed to compare the performance of different methods, the obtained calculation results are listed in Table 3. In addition, the theoretical solutions provided in [18] are also listed in this section. It can be observed that the results obtained

using linear elements Hex8 differ significantly from the theoretical solution. Conversely, the quadratic form Hex20 exhibits excellent computational precision and conforms closely to the theoretical solution. Furthermore, compared to Hex20, the results of SBFEM-Q with a quadratic mesh are closer to the theoretical solutions due to the advantages of SBFEM. Meanwhile, the solutions obtained by the proposed SBFEM-M also achieve good accuracy with a slightly larger deviation than SBFEM-Q, yet the total number of degrees of freedom has been reduced by 46.61 %. Therefore, it can be verified that the proposed method in this paper not only ensures good accuracy but also greatly reduces the amount of computation.

##### 4.2. Region-oriented order conversion approach of mixed elements

The advantage of mixed-order elements lies in their ability to allocate edges of different orders for calculation according to requirements, ultimately achieving an ideal state of high accuracy and efficiency. Nonetheless, manually setting the mixed order would be a cumbersome and complex process. Therefore, in this section, a so-called region-oriented element order conversion approach is introduced. The detailed introduction is as follows.

###### 4.2.1. Selection of optimized region

To be more specific, as shown in Fig. 8, the critical region A of the model, which can be the stress concentration zone or tension zone, will be designated as quadratic elements as required. Conversely, the relatively less significant region C can be assigned as linear elements, and the remaining connected region B is defined as mixed-order elements. The implementation process is achieved through a self-developed program.

###### 4.2.2. Thin curving beam model

A cantilever thick curving beam is subjected to a vertical force at the tip (Fig. 9), and two radius ratios, (i)  $R = 10$  m and (ii)  $R = 15$  m, are considered for the application of this approach. The thickness is defined as 1 m. The modulus  $E = 1.0 \times 10^9$  Pa, Poisson's ratio  $\nu = 0.333$ , and a shear load  $F = 1.0 \times 10^6$  N is applied on the free surface. At the fixed end, all degrees of freedom are restrained.

In Fig. 10, the model is discretized into 576 quadratic hexahedron elements with 3165 nodes, which is called "Quadratic mesh". As a comparison, a mesh with linear elements is also adopted, just as depicted in Fig. 11(b). Besides, the region-oriented order conversion approach is applied to the reallocation of element types. According to the research in [56], for such a cantilever beam, the coarse mesh with a focus on the outboard regions is sufficient to achieve a computational accuracy that matches the global fine mesh, thus the regions near the inner side of the beam are designated as quadratic hexahedron elements, while the other regions are linear form, thus two "Mixed-order mesh" are formed, as shown in Figs. 11(c) and 11(d).



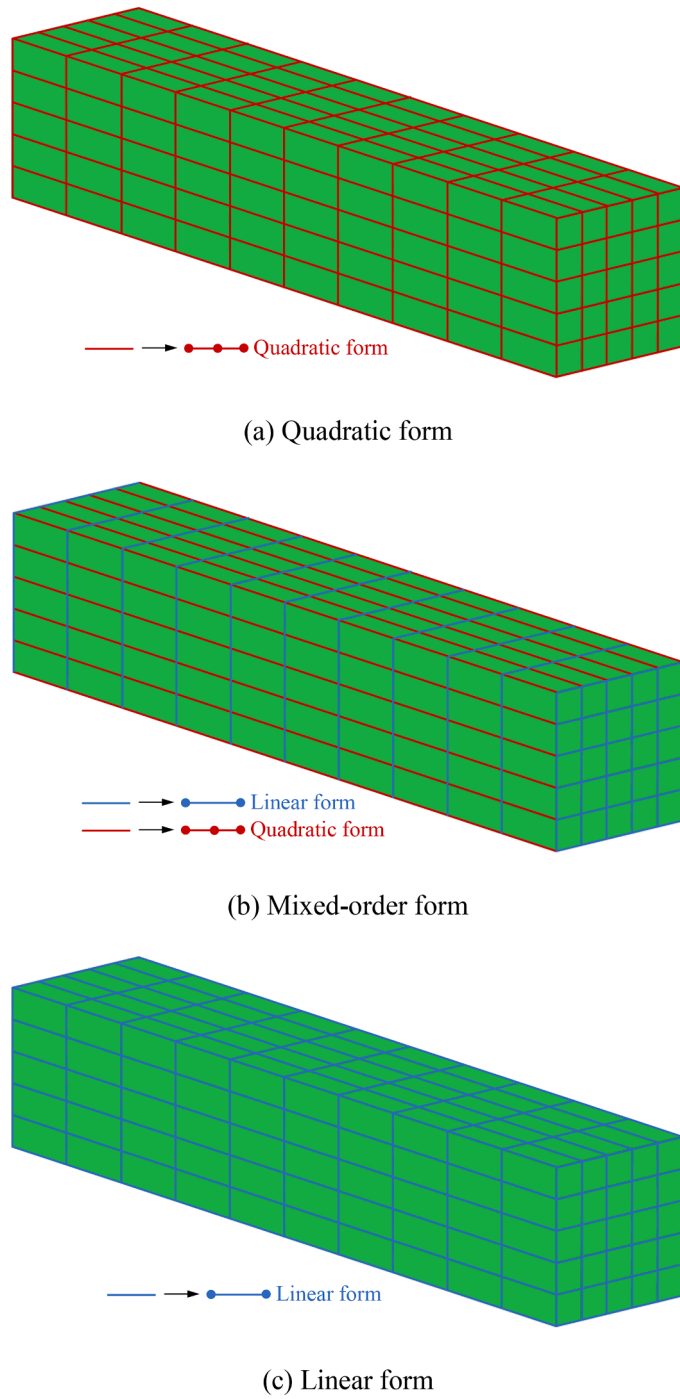


Fig. 7. The 3D mesh discretization of a cantilever beam.

#### 4.2.3. Calculation results

**4.2.3.1. Displacement analysis.** The calculations, which applied different mesh types, are carried out in this section. The obtained displacements of point A corresponding to different mesh types are listed in Table 4. It is seen that the displacement results using linear mesh maintain a large difference from the results of the quadratic mesh. On the contrary, mixed-order meshes show a good agreement with the solutions for the quadratic mesh, especially for mixed-order mesh 1, the obtained results can almost reach the calculation accuracy of the quadratic mesh, accompanied by errors of 2.38 % and 1.96 %, respectively. Meanwhile, the reduction of Dofs is particularly noticeable, meaning that the amount of computation is significantly reduced.

Table 2

Detailed information on different element types.

Element type	Element shape	Method description
Hex8		3D linear iso-parametric element calculated by FEM
Hex20		3D quadratic iso-parametric element calculated by FEM
SBFEM-Q		3D quadratic element calculated by SBFEM
SBFEM-M		Mixed-order element calculated by SBFEM (Note: The edge midpoints depicted in this element are only illustrative and it does not represent the actual node distribution in this example.)

Table 3

Displacement component-y of Point A in the cantilever beam.

Element Type	Mesh form	Load I		Load II	
		$u_y$	Error/%	$u_y$	Error/%
Hex8	linear	85.66	14.34	87.60	14.53
Hex20	quadratic	95.26	4.74	96.40	5.95
SBFEM-Q	quadratic	99.71	0.29	100.7	1.76
SBFEM-M	Mixed-order	97.93	2.07	99.57	2.86
Theory solution	—	100	—	102.5	—



Fig. 8. Schematic diagram of region-oriented order conversion approach.

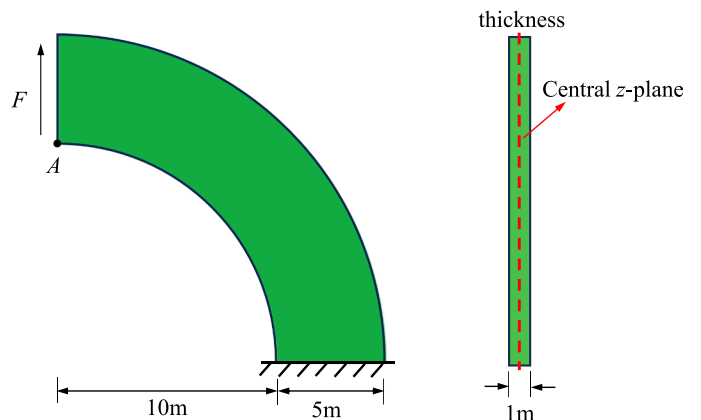


Fig. 9. Thin curving beam model.

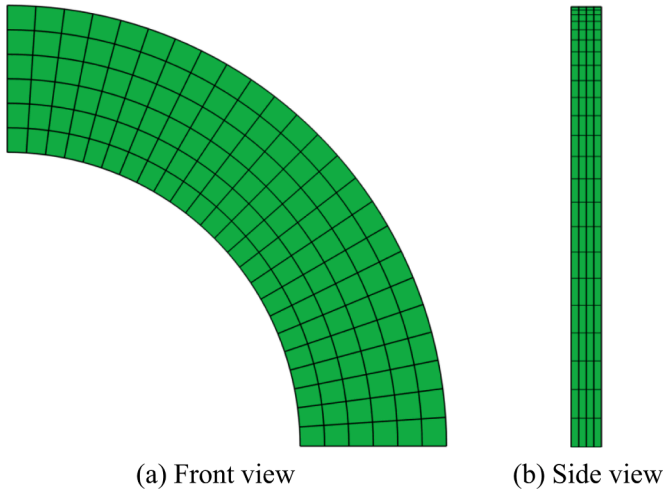


Fig. 10. The 3D mesh discretization of a thin curving beam.

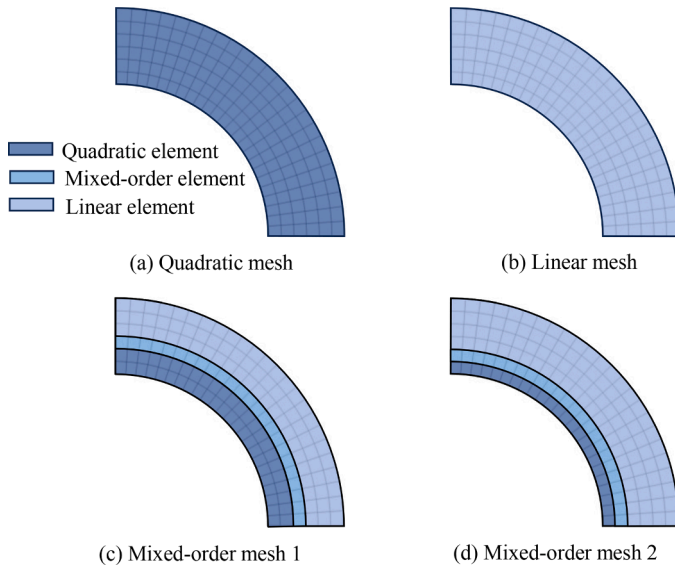


Fig. 11. Element type allocation schematics for different mesh type.

Table 4  
Displacements of Point A in the thin curving beam.

Mesh	$u_x$	$u_x$ error (%)	$u_y$	$u_y$ error (%)	Dofs	Dofs reduction (%)
Quadratic	0.377	–	0.868	–	9495	–
Linear	0.288	23.60	0.737	15.09	2625	–
Mixed-order 1	0.368	2.38	0.851	1.96	5355	43.60
Mixed-order 2	0.357	5.31	0.825	4.95	4320	54.50

The rule of displacement components  $x$  and  $y$  of the points on the inner side of the beam in the central  $z$ -plane corresponding to different mesh types are offered in Fig. 12. It can be seen from the figures that displacement results of the linear mesh differ significantly from the mesh with quadratic elements. However, the results of the mixed-order mesh agree very well with that of quadratic mesh, especially for the mixed-order mesh 1. Therefore, the calculation precision in displacements of the region-oriented order conversion approach can be preserved very well while significantly reducing computational costs.

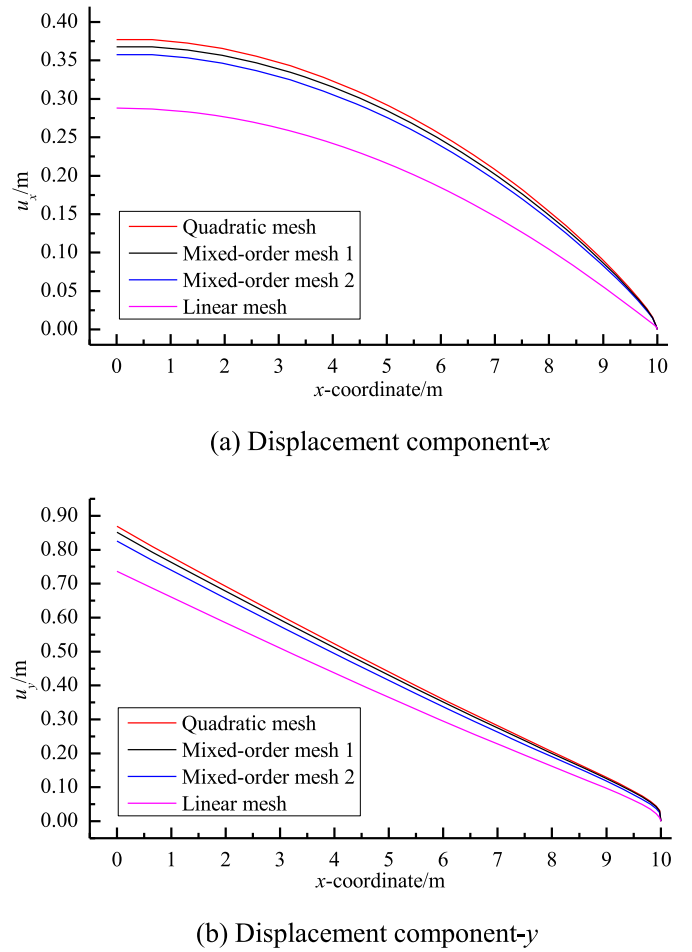


Fig. 12. Displacement rule on the inner side of the thin curving beam in the central  $z$ -plane.

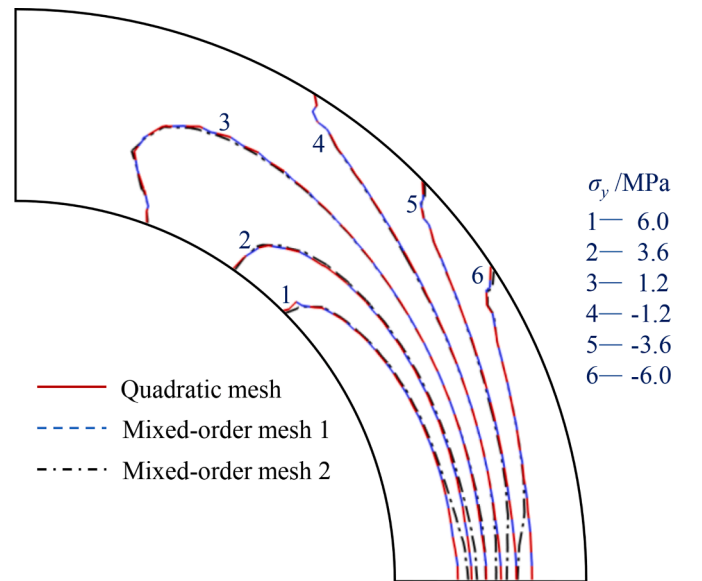


Fig. 13. The stress component  $\sigma_y$  of the thin curving beam in the central  $z$ -plane.

4.2.3.2. *Stress analysis.* Fig. 13 shows the stress component  $\sigma_y$  of the beam in the central  $z$ -plane for different mesh types, and it can be seen that  $\sigma_y$  are highest in magnitude at the inner side of the beam due to the



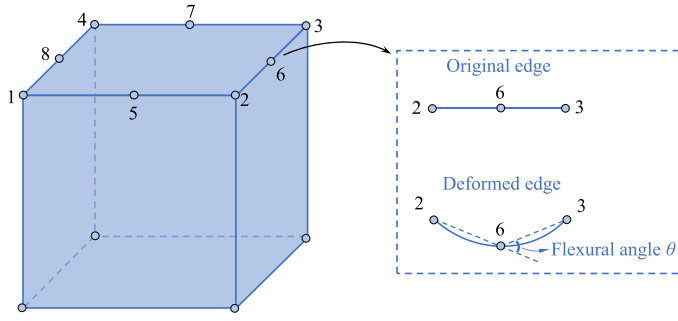


Fig. 14. Schematic diagram of the flexural angle of quadratic surface element.

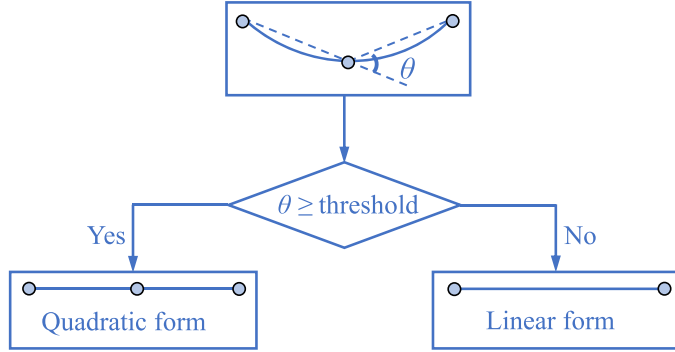


Fig. 15. Process diagram of automatic edge order conversion approach.

tension of shear load. Furthermore, the obtained stress rules based on mixed-order meshes can nearly reproduce the accuracy of the quadratic mesh. Specifically, the stress contour lines of mixed-order mesh 1 are essentially consistent with the quadratic mesh, thus the exactness of the order conversion approach of mixed elements in stress calculation is demonstrated.

#### 4.3. Automatic flexural angle-oriented order conversion approach

In Section 4.2, the order conversion approach is to select the critical region artificially depending on experience. In this way, although the order conversion of the element edges achieves a certain manual free, it is still not automated. Therefore, in this section, a flexural angle-oriented order conversion approach for different edge orders of hexahedron elements is provided for the bending structures. The specific introduction is as follows.

##### 4.3.1. Definition of flexural angle

The automatic conversion approach of mixed-order elements based on the flexural angle-oriented order conversion approach is shown in Fig. 14. The determination process is as follows: the calculation based on quadratic elements is first performed, and then the bending deformation occurs when the structure is subjected to external loads. The flexural angle  $\theta$ , which is shown in Fig. 14, can be determined by the vectors  $\vec{26}$  and  $\vec{36}$  sharing the common midpoint after deformation. Then, a threshold angle is selected. If  $\theta$  is less than the threshold, the bending effect experienced by the edge will be deemed to be inconspicuous, thus the quadratic form is not necessary, and the edge will be reduced to a linear form, as shown in Fig. 15; Otherwise, the edge will still be maintained as quadratic form. In this way, different orders can be automatically allocated on line elements.

##### 4.3.2. MBB beam example

In this example, a 3D MBB beam shown in Fig. 16 is studied to demonstrate the implementation process of this scheme. The bottom end

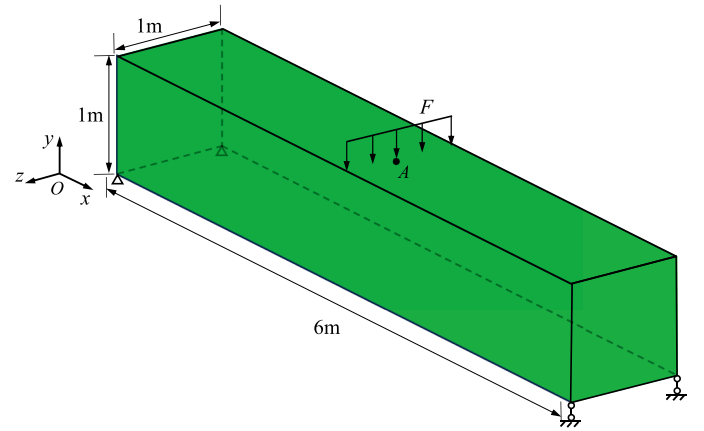


Fig. 16. 3D BMM beam model.

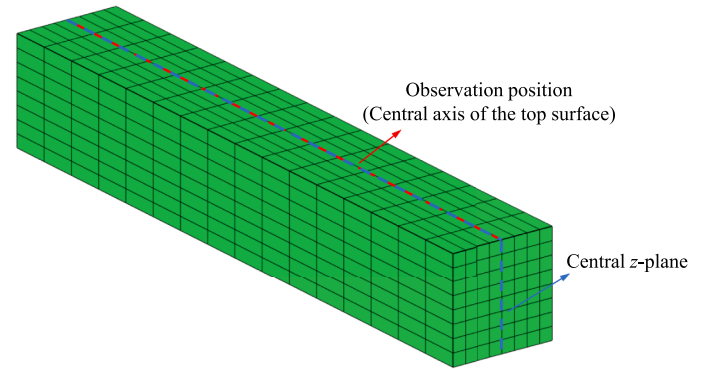


Fig. 17. The 3D mesh discretization of MBB beam.

of the beam is fixed while the middle of the top beam is subjected to a uniform force load  $F = 2 \times 10^6 \text{ N}$ . The dimensions of the 3D beam are: length = 6 m, width = 1 m, and height = 1 m; and elastic properties are: Young's modulus  $E = 3 \times 10^8 \text{ Pa}$ , Poisson's ratio  $\nu = 0.25$ . Quadratic hexahedron elements are first used to discretize the beam model, resulting in 1024 elements with 5121 nodes, as shown in Fig. 17.

##### 4.3.3. Calculation results

In this section, different mixed-order element schemes based on the flexural angle-oriented order conversion approach are applied to the calculation. To better demonstrate the properties of mixed-order elements, three different threshold angles including  $\theta = 0.2^\circ$ ,  $0.4^\circ$ , and  $0.6^\circ$  are selected in this simulation, the resulting mixed-order element allocation in the central z-plane of the beam is shown in Fig. 18. It can be seen from Fig. 18 that as  $\theta$  increases, more surface edges are reduced to linear form, and almost all vertical edges are reduced to linear, which is easy to understand as such edges hardly undergo bending deformation. Furthermore, in the case of  $\theta = 0.6^\circ$ , only the horizontal edges near the middle position remain in quadratic form.

The y-direction displacement  $u_y$  of point A, which is marked in Fig. 16, is listed in Table 5 to compare the performance of different allocation schemes. As shown in Table 5, the accuracy of the allocation schemes with different  $\theta$  can be nearly consistent with that of the quadratic element scheme, which is represented by  $\theta = 0^\circ$ . However, the degrees of freedom have been greatly reduced, indicating the proposed order conversion approach has excellent advantages in terms of accuracy and computation amount.  $u_y$  of the observation position in the central axis of the top surface, which is shown in Fig. 17, are extracted to further compare the performance of different schemes in Fig. 19. Obviously, the accuracy of the proposed order conversion approach is further confirmed, as curves corresponding to different  $\theta$  show very

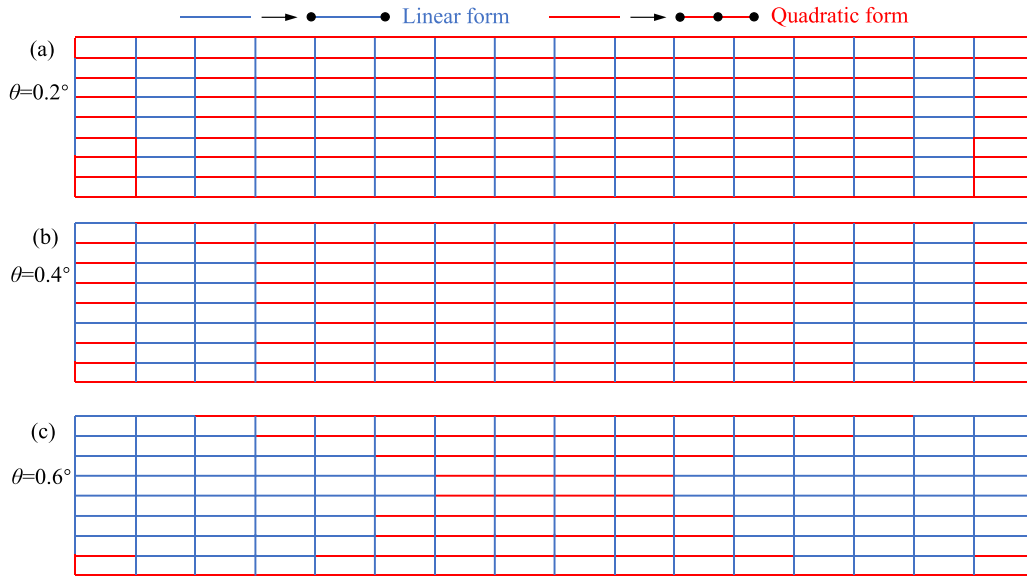


Fig. 18. Mixed-order element allocation with different  $\theta$  in the central  $z$ -plane.

Table 5

y-direction displacements of Point A in the cantilever beam.

$\theta$	$u_y$	$u_y$ error (%)	Dofs	Dofs reduction (%)
0° (Fully quadratic)	0.452	–	15,363	–
0.2°	0.448	0.88	10,410	32.24
0.4°	0.444	1.77	8292	46.03
0.6°	0.438	3.10	7188	53.21

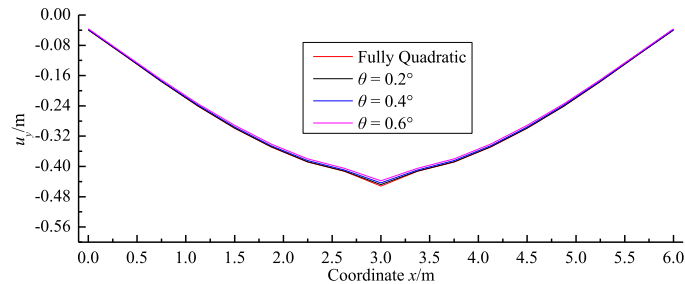


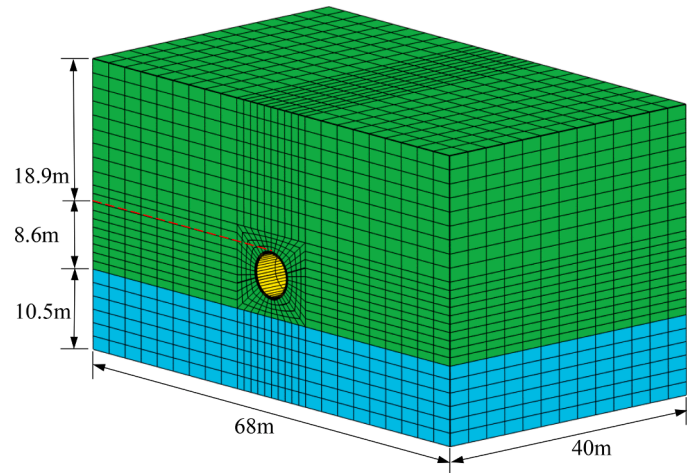
Fig. 19.  $u_y$  of the observation position in the top central axis.

small deviations.

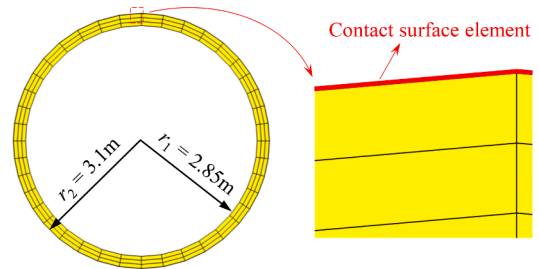
## 5. Engineering application

To demonstrate the applicability of the proposed method in engineering practice, an actual underground drainage tunnel (Fig. 20) is selected in this section. The tunnel is located in a soil layer, the overlying soil above the tunnel is 18.9 m high. A bedrock layer lies beneath the soil mass, and other detailed geometric information can be found in Fig. 20. A linear hexahedron mesh including 11,960 elements and 13,902 nodes is discretized for the model.

For the tunnel, it is discretized into 3-layer elements along the thickness direction. Between the tunnel and the soil, a thin layer of contact surface elements is arranged, just as shown in Fig. 20(b). During the analysis process, the behavior of overlying soil is assumed to conform to a generalized plastic model, and its parameters are listed in Table 6. The concrete for the tunnel lining and bedrock at the base are assumed to be elastic materials. Besides, joint elements are applied at the contact surface, and a generalized plastic contact surface model is



(a) Geometry and linear mesh discretization



(b) Tunnel mesh

Fig. 20. Overall information of the underground drainage tunnel.

Table 6

Generalized plasticity model parameters for the overlying soil.

$G_0$	$K_0$	$M_g$	$M_f$	$\alpha_f$	$\alpha_g$	$H_{u0}$	$H_{l0}$	$m_v$
470	1100	1.68	1.30	0.10	-0.4	1100	550	0.23
$m_l$	$m_s$	$\beta_0$	$\beta_1$	$\gamma_{DM}$	$r_d$	$\gamma_u$	$m_u$	
0.45	0.23	20	0.02	20	110	5	0.45	

**Table 7**

Generalized plastic interface model parameters.

$D_{s0}/\text{kPa}$	$D_{n0}/\text{kPa}$	$M_c$	$e_r$	$\lambda$	$a/\text{kPa}^{0.5}$	$b$	$c$
1000	1500	0.88	0.0	0.091	224	0.06	3.0
$\gamma_d$	$k_m$	$M_f$	$k$	$H_0/\text{kPa}$	$f_h$	$t/m$	$a$
0.2	0.6	0.65	0.5	8500	2.0	0.1	0.65

adopted [57], whose parameters are given in Table 7.

The displacement, deformation, and stress distribution contour of the tunnel are shown in Fig. 21. As can be seen in Fig. 21(a), the y-direction displacement  $u_y$  will occur at the top of the tunnel under the self-weight pressure of the overlying soil, and the corresponding deformation diagram is depicted in Fig. 21(b). In this deformation mode, a maximum tensile stress value of 0.156 MPa (Fig. 21(c)) is observed in element A located at the central position of the tunnel top, as shown in Fig. 22.

Furthermore, to seek a more accurate calculation result, a mixed-order scheme is executed. With the tunnel as the focus of attention, the elements around the tunnel are raised to the quadratic form, and most of the remaining elements remain in a linear form. The elements connecting two orders of elements are regarded as mixed-order elements, and the schematic diagram of the element allocation scheme in the cross-section is shown in Fig. 23(a). In addition, for comparison, a whole quadratic mesh is also included, as depicted in Fig. 23(b). Subsequently, simulation calculations based on the above two types of meshes are carried out.

The obtained tensile stress extreme values in element A for different

meshes are given in Table 8. Here, the result of the quadratic mesh is considered as a reference standard. As seen, due to the endowed local quadratic property, the mixed-order mesh can almost replicate the computational accuracy of a fully quadratic mesh with an error of 0.72 %; however, the Dofs have been drastically scaled down by 50.11 %. The linear mesh, on the other hand, obtains result that differ significantly from that of the quadratic mesh due to the volume-locking restriction. Based on this, it is reasonable to believe that a local quadratic mesh is highly desirable in regions dominated by bending or tension. Therefore, the practicality of the proposed method in this paper can be demonstrated.

## 6. Conclusion

This paper develops a flexible mixed-order hexahedron element based on SBFEM theory with the co-existence of linear and quadratic forms for boundaries, wherein the interpolation function for quadrilateral surface elements with multiple nodes is formulated through serendipity elements. In addition, two approaches oriented to the critical region and the flexural angle are employed to achieve the conversion of boundary orders. The rationality and accuracy of the proposed method are demonstrated with several numerical examples. The main conclusions of this paper are as follows:

- (1) A satisfactory accuracy and robustness performance is achieved via the proposed method. The obtained results are in good agreement with the theoretical and quadratic FEM solutions with

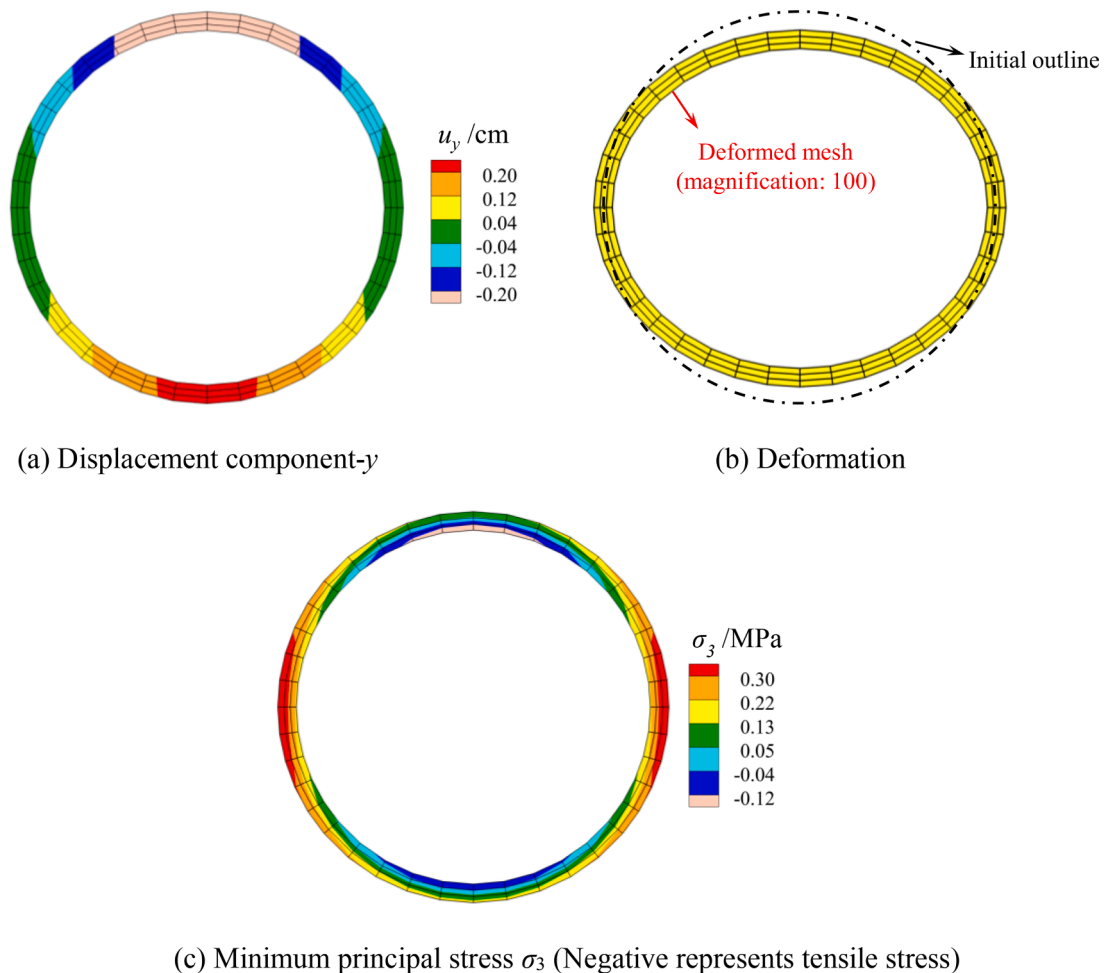


Fig. 21. The calculation results for the tunnel.

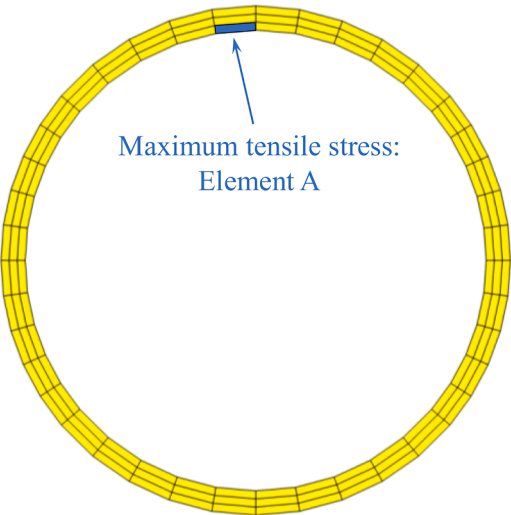


Fig. 22. Maximum tensile stress region.

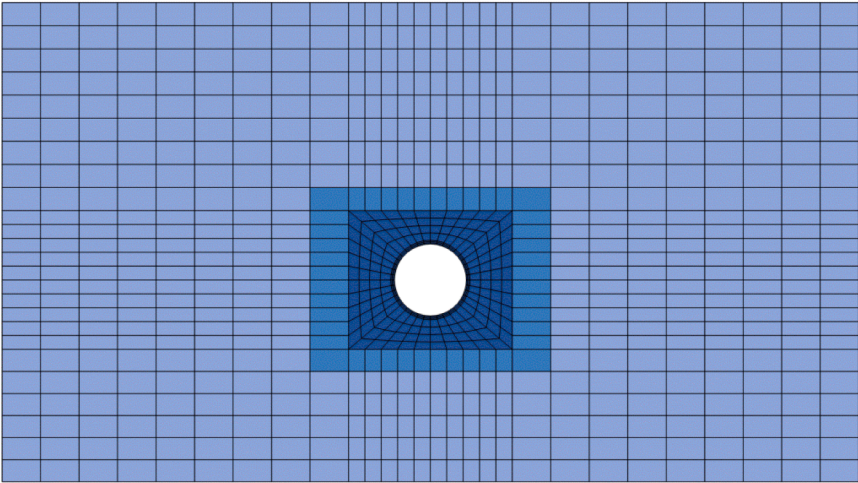
errors of less than 3 %, while the error for the linear element is about 15 %, thereby the proposed method is proven to be reliable.

(2) A significant improvement in the efficiency has been realized. The adoption of two order conversion approaches with less manual intervention ensures the proper arrangement of surface orders in hexahedron elements. In this way, unnecessary computations are circumvented, leading to a 40–55 % improvement in computational efficiency with minimal loss of accuracy. Meanwhile, satisfactory engineering applicability can also be achieved through the order conversion approach.

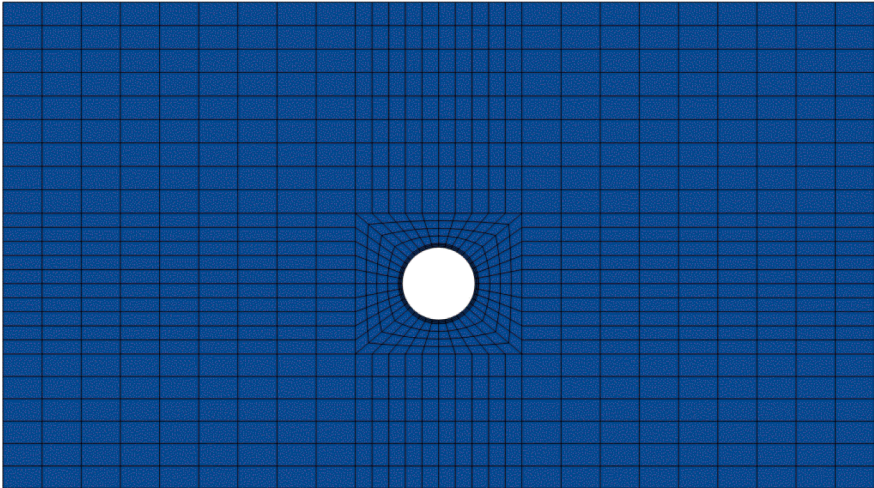
**Table 8**  
Comparison of results and Dofs between different meshes.

Mesh	Tensile stress in element A / MPa (error/%)	Dofs (reduction/ %)
Quadratic	0.277 (-)	152,619 (-)
Mixed-order (the proposed method)	0.275 (0.72)	76,146 (50.11)
Linear	0.156 (77.56)	41,706 (72.67)

■ Quadratic element   ■ Mixed-order element   ■ Linear element



(a) Mixed-order mesh



(b) Quadratic mesh

Fig. 23. Schematic diagram of different mesh allocation schemes in the cross-section.



The proposed method has the potential to be applied in reliability analysis to further enhance its practicality and expand its application scenarios, and this is also a focus of our future research.

### CRediT authorship contribution statement

**Xiupeng Nie:** Writing – original draft, Software, Methodology, Investigation. **Degao Zou:** Supervision, Software, Funding acquisition. **Kai Chen:** Writing – review & editing, Supervision, Data curation, Conceptualization. **Xianjing Kong:** Supervision, Resources. **Guoyang Yi:** Investigation, Conceptualization.

### Declaration of competing interest

The authors declare that they have no known competing financial interests or personal relationships that could have appeared to influence the work reported in this paper.

### Data availability

Data will be made available on request.

### Acknowledgments

This work was supported by the National Natural Science Foundation of China (Grant Nos. 52192674, 52350393, U2240211, 52109151).

### References

- Natarajan S, Ooi ET, Saputra A, Song C. A scaled boundary finite element formulation over arbitrary faceted star convex polyhedra. *Eng Anal Bound Elem* 2020;80:218–29. <https://doi.org/10.1016/j.enganabound.2017.03.007>.
- Dohrmann C, Heinstein M, Jung J, Critical S, Witkowski W. Node-based uniform strain elements for three-node triangular and four-node tetrahedral meshes. *Int J Numer Meth Eng* 2020;47(9):1549–68. [https://doi.org/10.1002/\(SICI\)1097-0207\(20000330\)47:9<1549::AID-NME842>3.0.CO;2-K](https://doi.org/10.1002/(SICI)1097-0207(20000330)47:9<1549::AID-NME842>3.0.CO;2-K).
- Gee M, Dohrmann C, Critical S, Wall W. A uniform nodal strain tetrahedron with isochoric stabilization. *Int J Numer Meth Eng* 2009;78(4):429–43. <https://doi.org/10.1002/nme.2493>.
- Zienkiewicz O, Humpheson C, Lewis R. Associated and non-associated viscoplasticity and plasticity in soil mechanics. *Geotechnique* 1975;25(4):671–89. <https://doi.org/10.1680/geot.1975.25.4.671>.
- Liu G, Quek S. *The Finite Element Method: A Practical Course*. Butterworth-Heinemann; 2013.
- Cheng Y, Zhang Y. Formulation of a three-dimensional numerical manifold method with tetrahedron and hexahedron elements. *Rock Mech Rock Eng* 2008;41:601–28. <https://doi.org/10.1007/s00603-006-0120-9>.
- Sukumar N, Moës N, Moran B, Belytschko T. Extended finite element method for three-dimensional crack modeling. *Int J Numer Meth Eng* 2000;48(11):1549–70. [https://doi.org/10.1002/1097-0207\(20000820\)48:11<1549::AID-NME955>3.0.CO;2-A](https://doi.org/10.1002/1097-0207(20000820)48:11<1549::AID-NME955>3.0.CO;2-A).
- Okada H, Higashi M, Kikuchi M, Fukui Y, Kumazawa N. Three dimensional virtual crack closure-integral method (VCCM) with skewed and non-symmetric mesh arrangement at the crack front. *Eng Fract Mech* 2005;72(11):1717–37. <https://doi.org/10.1016/j.engfracmech.2004.12.005>.
- Beyabanaki S, Jafari A, Biabanaki S, Yeung M. Nodal-based three-dimensional discontinuous deformation analysis (3-D DDA). *Comput Geotech* 2009;36(3):359–72. <https://doi.org/10.1016/j.compgeo.2008.08.009>.
- Dobrev V, Knupp P, Kolev T, Mittal K, Tomov V. hr-Adaptivity for nonconforming high-order meshes with the target matrix optimization paradigm. *Eng Comput* 2022;38:3721–37. <https://doi.org/10.1007/s00366-021-01407-6>.
- Romo E. 3D unsteady diffusion and reaction-diffusion with singularities by GFEM with 27-node hexahedrons. *Math Probl Eng* 2014;560492. <https://doi.org/10.1155/2014/560492>.
- Geelen R, Plews J, Tupek M, Dolbow J. An extended/generalized phase-field finite element method for crack growth with global-local enrichment. *Int J Numer Meth Eng* 2020;121(11):2534–57. <https://doi.org/10.1002/nme.6318>.
- Qu Y, Zou D, Chen K, Liu J. Three-dimensional refined analysis of seismic cracking and anti-seismic measures performance of concrete face slab in CFRDs. *Comput Geotech* 2021;139:104376. <https://doi.org/10.1016/j.compgeo.2021.104376>.
- Schmidt M, Noël L, Doble K, Evans J, Maute K. Extended isogeometric analysis of multi-material and multi-physics problems using hierarchical B-splines. *Comput Mech* 2023;71:1179–203. <https://doi.org/10.1007/s00466-023-02306-x>.
- Prathap G. The poor bending response of the four-node plane stress quadrilateral. *Int J Numer Meth Eng* 1985;21(5):825–35. <https://doi.org/10.1002/nme.1620210505>.
- Wan D, Hu D, Natarajan S, Bordas S, Long T. A linear smoothed higher-order CS-FEM for the analysis of notched laminated composites. *Eng Anal Bound Elem* 2017;85:127–35. <https://doi.org/10.1016/j.enganabound.2017.10.003>.
- Mannini A, Gaudenzi P. Multi-layer higher-order finite elements for the analysis of free-edge stresses in piezoelectric actuated laminates. *Compos Struct* 2003;61(3):271–8. [https://doi.org/10.1016/S0263-8223\(02\)00040-5](https://doi.org/10.1016/S0263-8223(02)00040-5).
- Taylor R, Beresford P, Wilson E. A non-conforming element for stress analysis. *Int J Numer Meth Eng* 1976;10(6):1211–9. <https://doi.org/10.1002/nme.1620100602>.
- Zlámal M. Superconvergence and reduced integration in the finite element method. *Math Comput* 1978;32(143):663–85. <https://doi.org/10.1090/s0025-5718-1978-0495027-4>.
- Taylor R. On completeness of shape functions for finite element analysis. *Int J Numer Meth Eng* 1972;4(1):17–22. <https://doi.org/10.1002/nme.1620040105>.
- Wachspress E. Incompatible quadrilateral basis functions. *Int J Numer Meth Eng* 1978;12(4):589–95. <https://doi.org/10.1002/nme.1620120404>.
- Pian T, Suhmura K. Rational approach for assumed stress finite elements. *Int J Numer Meth Eng* 1984;20(9):1685–95. <https://doi.org/10.1002/nme.1620200911>.
- Rajendran S. Optimal stress recovery points for higher-order bar elements by Prathap's best-fit method. *Commun Numer Meth Eng* 2009;25(8):864–81. <https://doi.org/10.1002/cnm.1129>.
- Zalmal M. A remark on the 'Serendipity family'. *Int J Num Meth Engng* 1973;7(1):98–100. <https://doi.org/10.1002/nme.1620070109>.
- Ball A. The interpolation function of a general serendipity rectangular element. *Int J Num Meth Engng* 1980;15(5):773–8. <https://doi.org/10.1002/nme.1620150512>.
- Crum J, Cheng C, Ham D, Mitchell L, Kirby R, Levine J, Gillette A. Bringing trimmed serendipity methods to computational practice in firedrake. *Acm T Math Software* 2022;48(1):1–19. <https://doi.org/10.1145/3490485>.
- Song C, Wolf J. The scaled boundary finite-element method-alias consistent infinitesimal finite-element cell method-for elastodynamics. *Comput Method Appl Mech Eng* 1997;147(3–4):329–55. [https://doi.org/10.1016/S0045-7825\(97\)00021-2](https://doi.org/10.1016/S0045-7825(97)00021-2).
- Song C. Dynamic analysis of unbounded domains by a reduced set of base functions. *Comput Method Appl Mech Eng* 2006;195(33/36):4075–94. <https://doi.org/10.1016/j.cma.2005.07.011>.
- Song C, Ooi E, Natarajan S. A review of the scaled boundary finite element method for two-dimensional linear elastic fracture mechanics. *Eng Fract Mech* 2017;187:45–73. <https://doi.org/10.1016/j.engfracmech.2017.10.016>.
- Song C, Zhang X. High-order composite implicit time integration schemes based on rational approximations for elastodynamics. *Comput Method Appl Mech Eng* 2024;418:116473. <https://doi.org/10.1016/j.cma.2023.116473>.
- Zhang J, Ankit A, Gravenkamp H, Eisentragner S, Song C. A massively parallel explicit solver for elasto-dynamic problems exploiting octree meshes. *Comput Method Appl Mech Eng* 2021;380:113811. <https://doi.org/10.1016/j.cma.2021.113811>.
- Zhang J, Zhao M, Eisentragner S, Du X, Song C. An asynchronous parallel explicit solver based on scaled boundary finite element method using octree meshes. *Comput Method Appl Mech Eng* 2022;401:115653. <https://doi.org/10.1016/j.cma.2022.115653>.
- Zhang J, Wang P, Zhao M, Liu L, Qu Y, Du X. A scaled boundary finite element method for soil dynamic impedance of pile groups using hybrid quadtree mesh considering horizontal vibration. *Eng Anal Bound Elem* 2023;153:226–41. <https://doi.org/10.1016/j.enganabound.2023.05.029>.
- Du C, Huang W, Ghaemian M, Jiang S, Zhao Z. New nonlocal multiscale damage model for modelling damage and cracking in quasi-brittle materials. *Eng Fract Mech* 2023;277:108927. <https://doi.org/10.1016/j.engfracmech.2022.108927>.
- Shen X, Du C, Jiang S, Zhang P, Chen L. Multivariate uncertainty analysis of fracture problems through model order reduction accelerated SBFEM. *Appl Math Model* 2024;125:218–40. <https://doi.org/10.1016/j.apm.2023.08.040>.
- Jiang S, Deng W, Ooi E, Sun L, Du C. Data-driven algorithm based on the scaled boundary finite element method and deep learning for the identification of multiple cracks in massive structures. *Comput Struct* 2024;291:107211. <https://doi.org/10.1016/j.compstruc.2023.107211>.
- Zhao M, Liu P, Zhang J, Zhang G, Gao Z, Du X. A direct time-domain FEM-SBFEM-SBPML method for soil-structure interaction analysis using quadtree mesh. *Comput Geotech* 2023;161:105597. <https://doi.org/10.1016/j.compgeo.2023.105597>.
- Zhang G, Zhao M, Zhang J, Du X. Scaled Boundary Perfectly Matched Layer (SBPML): a novel 3D time-domain artificial boundary method for wave problem in general-shaped and heterogeneous infinite domain. *Comput Method Appl Mech Eng* 2023;403:115738. <https://doi.org/10.1016/j.cma.2022.115738>.
- Zhang G, Zhao M, Du X, Zhang J. Time-domain scaled boundary perfectly matched layer for elastic wave propagation. *Int J Numer Meth Eng* 2023;124(18):3906–34. <https://doi.org/10.1002/nme.7300>.
- Zhang G, Zhao M, Zhang J, Wang J, Du X. Scaled boundary perfectly matched layer for wave propagation in a three-dimensional poroelastic medium. *Appl Math Model* 2024;125:108–38. <https://doi.org/10.1016/j.apm.2023.09.028>.
- Zhang W, Li D, Zhang J, Guo X. Minimum length scale control in structural topology optimization based on the Moving Morphable Components (MMC) approach. *Comput Methods Appl Mech Eng* 2016;311:327–55. <https://doi.org/10.1016/j.cma.2016.08.022>.
- Zhang W, Xiao Z, Liu C, Mei Y, Youn S, Guo X. A scaled boundary finite element based explicit topology optimization approach for three-dimensional structures. *Int J Numer Meth Eng* 2020;121(21):4878–900. <https://doi.org/10.1002/nme.6498>.
- Ye W, Zang Q, Liu J, Yang F, Lin G. Three-dimensional bending and free vibration analyses of laminated cylindrical panel with/without elastic foundation using two-



- dimensional discrete method. *Soil Dyn Earthq Eng* 2023;168:107831. <https://doi.org/10.1016/j.soildyn.2023.107831>.
- [44] Zang Q, Liu J, Ye W, Yang F, Pang R, Lin G. High-performance bending and buckling analyses of cylindrical shells resting on elastic foundation using isogeometric scaled boundary finite element method. *Eur J Mech A* 2023;100:105013. <https://doi.org/10.1016/j.euromechsol.2023.105013>.
- [45] Chen K, Zou D, Tang H, Liu J, Zhuo Y. Scaled boundary polygon formula for Cosserat continuum and its verification. *Eng Anal Bound Elem* 2021;126:136–50. <https://doi.org/10.1016/j.enganabound.2021.02.007>.
- [46] Chen K, Zou D, Kong X, Chan A, Hu Z. A novel nonlinear solution for the polygon scaled boundary finite element method and its application to geotechnical structures. *Comput Geotech* 2017;82:201–10. <https://doi.org/10.1016/j.compgeo.2016.09.013>.
- [47] Chen K, Zou D, Kong X, Yu X. An efficient nonlinear octree SBFEM and its application to complicated geotechnical structures. *Comput Geotech* 2018;96:226–45. <https://doi.org/10.1016/j.compgeo.2017.10.021>.
- [48] Zhang G, Zhao M, Du X, Zhang J. Time-domain scaled boundary perfectly matched layer for elastic wave propagation. *Int J Numer Meth Eng* 2023;124(18):3906–34. <https://doi.org/10.1002/nme.7300>.
- [49] Zhang J, Eisentrger S, Zhan Y, Saputra A, Song C. Direct point-cloud-based numerical analysis using octree meshes. *Comput Struct* 2023;289:107175. <https://doi.org/10.1016/j.compstruc.2023.107175>.
- [50] Nie X, Chen K, Zou D, Kong X, Liu J, Qu Y. Slope stability analysis based on SBFEM and multistage polytree-based refinement algorithms. *Comput Geotech* 2022;149:104861. <https://doi.org/10.1016/j.compgeo.2022.104861>.
- [51] Qu Y, Eisentrger S, Zhang Z, Zhang L, Song C. Development of a fully automatic damage simulation framework for quasi-brittle materials. *Eng Anal Bound Elem* 2023;157:578–95. <https://doi.org/10.1016/j.enganabound.2023.10.004>.
- [52] Chen K, Zou D, Liu J, Zhuo Y. A high-precision formula for mixed-order polygon elements based on SBFEM. *Comput Geotech* 2023;155:105209. <https://doi.org/10.1016/j.compgeo.2022.105209>.
- [53] Barrett K. Multilinear Jacobians for iso-parametric planar elements. *Finite Elem Anal Des* 2004;40(8):821–53. [https://doi.org/10.1016/S0168-874X\(03\)00116-1](https://doi.org/10.1016/S0168-874X(03)00116-1).
- [54] Deeks A, Wolf J. A virtual work derivation of the scaled boundary finite-element method for elastostatics. *Comput Mech* 2002;28:489–504. <https://doi.org/10.1007/s00466-002-0314-2>.
- [55] Zou D, Liu J, Chen K. Theoretical introduction and operation instructions of the finite element high performance analysis software system for large geotechnical engineering. Dalian: Dalian University of Technology Press; 2018.
- [56] Ooi E, Saputra A, Natarajan S, Ooi E, Song C. A dual scaled boundary finite element formulation over arbitrary faceted star convex polyhedra. *Comput Mech* 2020;66:27–47. <https://doi.org/10.1007/s00466-020-01839-9>.
- [57] Liu J, Zou D, Kong X. A three-dimensional state-dependent model of soil–structure interface for monotonic and cyclic loadings. *Comput Geotech* 2014;61:166–77. <https://doi.org/10.1016/j.compgeo.2014.05.012>.